Compact and Sensitive H-Shaped Metal–Dielectric–Metal Waveguide Plasmonic Sensor

Rammani Adhikari[1,2] · Zen Sbeah[1] · Rahul Gupta[1,4] · Diksha Chauhan[1] · Jean-Michel Nunzi[3] ·
Ram Prakash Dwivedi[1]

Abstract

In this study, we designed and evaluated a sensing architecture using a metal–insulator-metal waveguide connected to an H-shape resonator for refractive index change measurement in two unique bands of refractive index: $n = 1.8$–1.95 and $n = 2.1$–2.3. A 3-D finite element approach is used to investigate the device sensing characteristics. For the waveguide, the H-shape resonator offers a cavity resonance zone where the substance to be detected is filled. The transmission curve plot revealed that the suggested arrangement generates two resonant dips. The resonant wavelength was found to have a direct and linear relationship with the refractive index of the material being sensed, the length of vertical height, and the width of the cavity's mid-arm. Sensitivity and figure of merit have the highest values of 1007.78 nm/RIU and 29 RIU^{-1}, respectively. The highest quality-factor obtained was 60. The proposed structure can be employed for refractive index sensing at the nanometer scale and increasing spectroscopy applications since it has features like nano size, high sensitivity, a linear relationship between tuning parameters, and a larger sensing span.

Keywords Cavity resonance · Fabrication defects · H–shape cavity · Lorentzian resonance · Refractive index sensor · Sensitivity

Background

Plasmonic is a branch of nano-optics that makes use of surface waves for propagating signals inside the waveguide. Those surface electromagnetic (EM) waves are named surface plasmon polaritons (SPPs) which travel across a metal–dielectric interface [1, 2]. Nowadays, SPPs based designs have drawn much attention of the researchers because they pose a remarkable ability to overcome the diffraction limit of light [3]. This exclusive feature provides a platform to design nano-sized devices which may have great potential application areas and maybe fit in realizing highly integrated optical circuits. For instance, plasmonic filters [4, 5], sensors [6], and optical switches [7] have been designed to exploit SPPs. Moreover, a special arrangement of metal–insulator-metal (MIM) layers is done to form a waveguide that relies on the propagation of SPPs in the core of the waveguide (WG). The MIM-WG construction has a non-conducting layer inserted between the dual conductor layers. Recently, the MIM-WG have attracted the mind of researchers because it offers many advantages like deep-subwavelength confinement of light needed for small-sized device, low loss of signal inside the core and surrounding, and relatively easy fabrication procedure needed to realize the design [8, 9]. With these features, they are used to model numerous optoelectronics devices that include filters [10–13], optical switches [12], demultiplexers [14], modulators [15, 16], coupler, and splitters [17, 18]. Recently, sensors based on SPP waves of MIM-WG are used for measuring the small variations of the refractive index (RI) of various substances. For example, these sensors are deployed in diverse application fields like the agriculture

✉ Ram Prakash Dwivedi
rp.dwivedi@gmail.com

1 Faculty of Engineering and Technology, Shoolini University, Bajhol, (HP) 173229, India

2 School of Engineering, Pokhara University, Pokhara Metropolitan City -30, Kaski, Nepal

3 Department of Physics, Engineering Physics, and Astronomy, Queen's University, Kingston, ON K7L-3N6, Canada

4 Department of Electrical and Electronics Engineering, Maharaja Agrasen University, Baddi, Solan, Himachal Pradesh, India

industry for sensing pesticides, the food industry for sensing chemicals, environmental monitoring by sensing gases and temperature, and biomedical instrumentations for detecting biochemicals and biological cells based on the refractive index (RI) change measurement. Such huge uses are because of their local field enrichment and top susceptibility to the nearby media. Scientists have labored to design, analyze and realize plasmonic sensors that are actually constructed with MIM-WGs and some coupled resonators. They have proposed numerous such structures. These structures rely on MIM-WG platform to exploit the features of Lorentzian resonances modes [6, 19–23], and Fano resonances (FRs) modes [24–32].

Research has demonstrated that structures based on meta-materials that act as an absorber to be used as sensing applications are just as important as MIM-WGs-based designs. They work with the concept of plasmonic resonance. A hyperbolic metamaterial, for example, works primarily on the same resonance principle in the terahertz and visible frequency bands, with only a few exceptions in the near-infrared frequency region [33]. They can also exploit the electromagnetic-induced transparency and plasmon-induced transparency which can be easily tuned and controlled to act as biosensors. They work on the principle of local-ized surface plasmon resonance. The metamaterial-relied absorbers are generally made up of gold, silver, platinum, titanium, chromium, and indium antimonides. These metals are expensive if we wish to achieve huge absorptivity in the visible and near-infrared regimes of the light wave. This problem can be solved by using tungsten – a cost-effective metamaterial [34]. The metamaterial absorber can be built utilizing nickel as a plasmonic material in the top layer for functioning in the UV to IR light regime, which has a prom-ising and steady absorption response [35]. The Yagi-Uda shaped metamaterial-based absorber is meant to function in the microwave regime's X- and Ku-bands, with ultra-small dimensions, controllable polarization, and incidence angle stability over a wide range of incidence angles [36]. Due to its superior performance, such as design flexibility, and ease of fabrication, on one hand, metal–insulator-metal-based metamaterial absorbers have recently become the most promising and explored for a wide range of wavelengths. MIM-WG-based devices, on the other hand, have attracted attention in the same way that metamaterials-based absorb-ers have. The focus of this paper is the latter one.

The exploitation of resonances in the MIM WG-cavity structure has opened the door for many optical applications. FR modes would be achieved in composite different resona-tors structures [37] whereas Lorentzian responses would be achieved both in single resonator structures and composite resonator structures [38]. The single resonator structures exploiting Lorentzian modes are rectangular cavity resona-tor [6], ring resonator [19], hexagonal cavity resonator [39],

fillet cavity resonator [40], hexagonal ring cavity resonator [41], square ring resonator [42, 43], ring-shaped Si resonator [44], half ring resonator [45], triangular ring and cavity reso-nators [46], and bow-tie cavity resonator [23]. The results of the above-discussed single resonator layouts revealed that the execution of resonators can further be increased with structural modifications. Moreover, it is observed that the performance enhancement is not only possible by structural design alone. So, there is still a room for the novel single structure that can provide acceptable sensitivity with sim-ple and smaller construction needed for fabrication. The proposed device may be one of the promising theoretical designs.

A very sensitive plasmonic architecture made up of a MIM-WG and an H–shaped cavity has been proposed and examined in this paper. The 3-D design was modeled with scattering boundary conditions. The finite element method (FEM) has been adopted to look into the performance of the presented structure. In designing and simulation, we use the commercially available software COMSOL Multiphysics. The transmission characteristics of the H-cavity are theoreti-cally investigated. In addition, the influences of structural parameters like vertical length, the width of the central arm, and separation between the two vertical legs of H – structure on the transmission curves and finally on overall sensing performances are investigated. The chemicals and liquids that have RIs between 1.8–1.95 and 2.1–2.3 are sensed and analyzed by varying the design parameters. This novel design is very compact size with a nanoscale footprint of $180nm \times 400nm \times 150nm$, easily fabricable, and offers excel-lent sensing performances. The design performs in the near-infrared regime where a halogen lamp or superluminescent diode (SLED) can act as the light source.

Design Model and Theory

As depicted in Fig. 1a, the proposed senor consists of a MIM-WG, where air (white part) acts as dielectric to con-struct the WG core (with width = 50 nm), and silver (Ag) (gray part) as metal. The H-shape cavity is placed tan-gentially on one side of the main WG to act as a cavity-resonator. The 3-D view of the proposed sensor structure is as shown in Fig. 1b. The H-cavity can be thought of as having three physical components two vertical legs and one horizontal arm named here as a middle or central arm. The structural parameters of the design, their notations, and their values are summarized in Table 1. The parameters are cho-sen to obtain better resonances obeying the resonant condi-tion specified by Eq. (6) and better sensing performances.

In the simulation, the structural parameters are set as $w = 50nm$, $l_1 = 330nm$ through 360 nm with an incre-ment of step size of 30 nm, $l_2 = 150nm$ through 165 nm
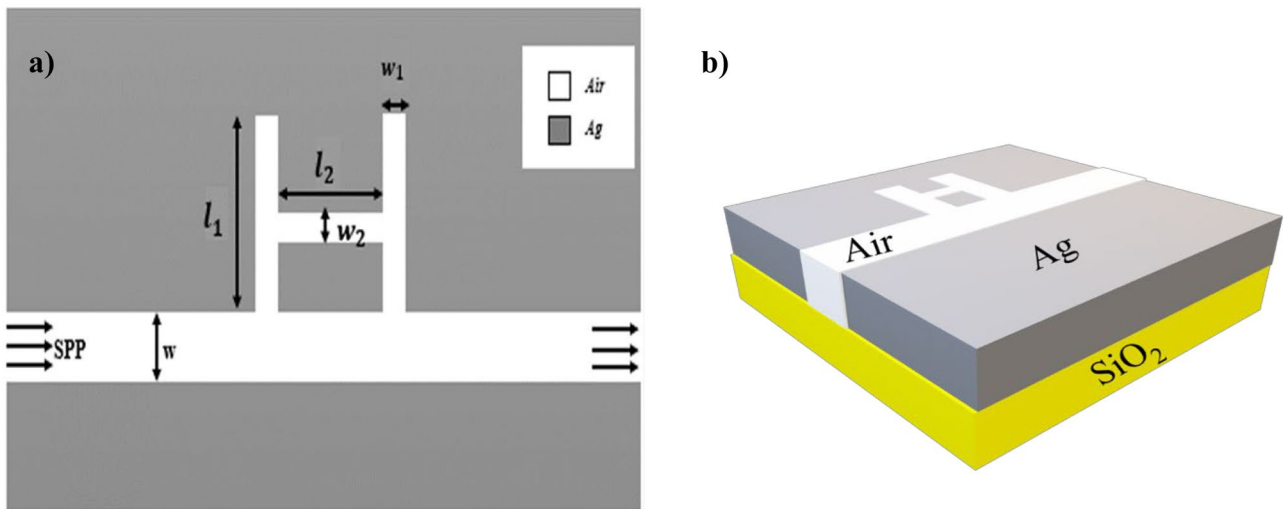
Fig. 1 **a** Schematic depiction of the proposed layout in two dimensions and **b** 3-D view of the proposed design.

by stepping of 5 nm, $w_1 = 30$nm, and $w_2 = 30$nm through 60 nm with an increment of step size of 10 nm. Throughout the simulation, w and w_1 are kept to their displayed values. Furthermore, the height of the design is fixed at 160 nm.

The lightwave excites SPPs that propagate across the center core of the waveguide which is then coupled to the cavity resonator, thus, generating a resonant condition. The electromagnetic field pattern is observed from the output port of the WG. One after another, the materials under sensing (MUS) are filled into the H-shape cavity. In doing so, the effective refractive index of the sensor gets changed which leads to wavelength shift at the output signal. The way of measuring the changes in wavelength swift as a result of changing filling materials (or optical RI of the medium) is called the wavelength interrogation technique which is the interrogation method used for the proposed sensor. The material-filled and lightwave interact with each other. At some particular wavelength, maximum interaction takes place and this wavelength is called the resonant wavelength. At the resonance condition, the power transfer to the output port is minimum and it is maximally captured in the cavity. The transmittance is calculated at this condition at the output port. For each RIs, transmission is calculated to demonstrate the resonance shift and calculate the performance parameters.

The suggested WG's size of 50 nm indicates that it is less than the magnitude of the light wave sent into it, ensuring that only the fundamental transverse magnetic (TM) mode propagates in the WG core. The primary TM mode has the following dispersion relation in the proposed MIM WG [19].

$$\epsilon_{in}k_{z2}\epsilon_m k_{z1}\coth\left(\frac{ik_{z1}\omega}{2}\right) = 0 \tag{1}$$

where k_{z1} and k_{z2} are momentum conservations and are defined as:

$$k_{z1}^2 = \epsilon_{in}k_0^2 - \beta^2 \tag{2}$$

$$k_{z2}^2 = \epsilon_m k_0^2 - \beta^2 \tag{3}$$

where $\epsilon_{in} = n^2$ is the insulator dielectric constant, β is the propagation constant, and $k_0 = 2\pi/\lambda_0$ is the vacuum wavevector. Ag is selected as the proposed WG's cladding layers due to its low absorption and low power consumption compared to other metals (gold and aluminum-like), as well as its ease of fabrication and strong etch selectivity [47]. Furthermore, Ag is regarded as one of the best metals for plasmonic applications in visible and near-infrared light, with excellent atmospheric stability and the lowest loss

Name of the parameter	Notation	Values (nm)
Width of the main WG	w	50 (fixed)
Length of the vertical cavities	l_1	330–360 (varied with the stepping of 10 nm)
Length of the horizontal cavity	l_2	150–165 (Varied with the stepping of 5 nm)
Width of the vertical cavities	w_1	30 (fixed)
Width of the horizontal cavity	w_2	30–60 (varied with the stepping of 10 nm)

Table 1 Dimensional summary of the proposed design

among all metals [48]. Ag is cheaper than Au and produces better outcomes. As a result, Ag is widely used, and it is employed here as well. For parameterization of the optical properties of Ag, Lorentz–Drude model is used which expresses its permittivity in terms of frequency by the following relation [42]:

$$\epsilon_m = \epsilon_\infty - \frac{\omega_p^2}{\omega(\omega + i\gamma)} \tag{4}$$

The symbols have their meanings such as Ag's dielectric constant $\epsilon_\infty (= 3.7)$ for infinite frequency, mass plasma frequency $\omega_p (= 9.1 ev)$ of loose moving electrons, $\gamma (= 0.018 ev)$ is the frequency that arises due to electrons collision, and ω is the angular frequency of fed light in vaccum.

The incident wave is partially reflected and partly coupled to the cavity resonator before being sent out of the output port. Only when the requirement of co-phased is met can a stable standing wave be built within the H-cavity [40]. The phase-matching condition is given by the following relation:

$$\Delta\varphi = 2\pi m (m = 1, 2, 3 \ldots \ldots .) \tag{5}$$

where m is the integer which indicates the mode number and $\Delta\varphi$ is the accumulative phase shift of SPP wave. At a certain wavelength of the signal, maximum interaction between EM wave and material filled in the cavity occurs, which indicates the resonance condition. At this condition, the minimum power transmission takes place which can be viewed from the output port. The resonant wavelength (λ_{res}) is expressed as [49]:

$$\lambda_{res} = \frac{2Ln_{eff}}{n - \frac{\varphi_{ref}}{\pi}} \tag{6}$$

where L is the cavity effective length, n_{eff} is the real component of the material media's resultant RI, and φ_{ref} is the phase swift due to reflections of SPPs in the interface of cavity-metal.

Simulations and Outcomes

We modeled and simulated the proposed layout using the platform of COMSOL Multiphysics software. 3-D FEM simulations are executed for numerical analysis. To soak up the energy of the escaping electromagnetic field, the model was designed by combining the properties of an RF module embedded in the electromagnetic (rfw) segment with scattering boundary conditions on all simulation range frontiers. Among the three TM mode components (E_x, E_y, and H_z), only the electric field components in the y-direction (E_y) linked with the SPP fundamental mode is considered. The electric field patterns (in the y-direction) are depicted in the middle of the dielectric's core. At both the input and output ports, the boundary integration approach is used to determine the input and output powers. The transmittance is then calculated by taking the ratio of these two powers as defined
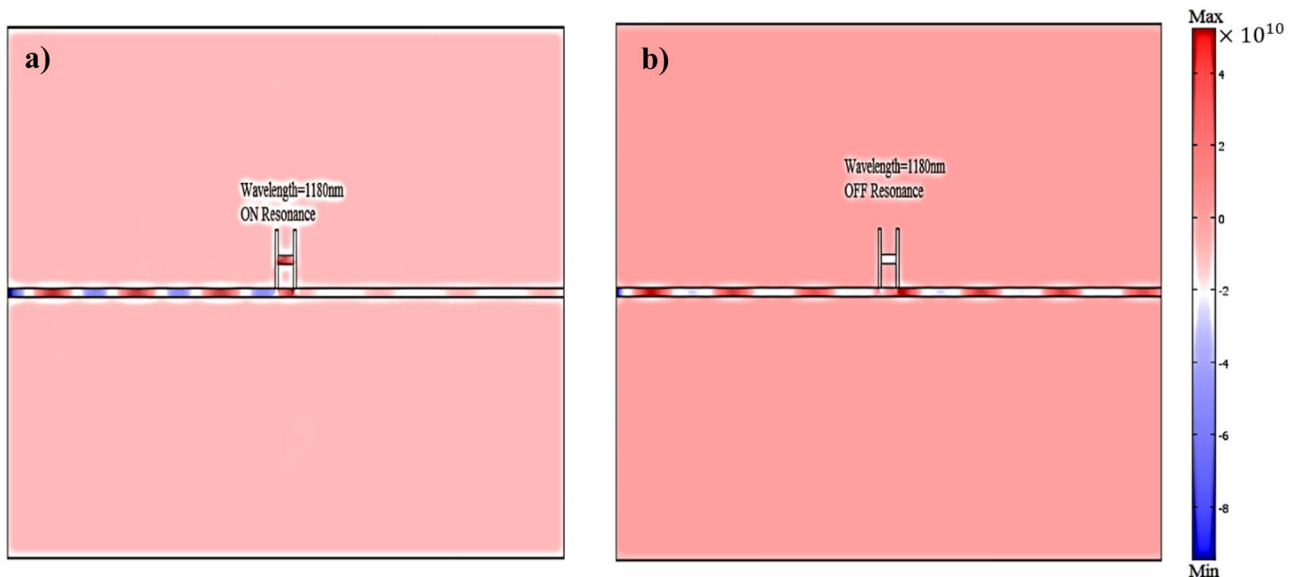
Fig. 2 Electric filed intensity pattern **a** for material having RI = 1.8 at wavelength = 1180 nm and **b** for material having RI = 1.85 at wavelength = 1180 nm

by the relation $T = P_{out}/P_{in}$, where P_{out} is the output power and P_{in} is the input power.

To verify the resonance and its shifting, the electric field patterns are plotted as shown in Fig. 2. Accordingly, all the light intensity has accumulated in the horizontal middle arm of the H–cavity at the λ_{res} (1180 nm) (Fig. 2a) when the medium under the cavity is having an RI of 1.8. However, when the material having RI of 1.85 is placed in the cavity, the different electric field pattern as shown in Fig. 2b is observed at the same wavelength of 1180 nm. At this condition, the electric field pattern is maximally confined within the main WG. This clearly shows that there are different resonance wavelengths for different materials. As a result, at resonance, the maximum power of the SPPs propagating in the WG is linked with an H-shape resonator. In contrast, only a tiny portion of the SPPs energy is coupled to the cavity resonator, whereas the majority of the energy that is not coupled to the resonator goes straight to the exit port under non-resonance conditions. The electric field patterns exhibit a standing wave profile both inside the cavity and waveguide in either of the conditions, i.e., at resonance and non-resonance.

The λ_{res} shifts can also be best explained with the help of the transmission curve. Once the materials are filled in the cavity, in turn, the light-matter interaction takes place resulting in the resonant condition as defined by Eq. (6). The resonant wavelengths observed are as follows: $\lambda_{res1} = 1045nm$ and $\lambda_{res2} = 1338nm$ when a material having RI = 1.8 is placed in the cavity for dip 1 and dip 2, respectively. For material having the RI = 1.85, the resonant wavelengths are as follows: $\lambda_{res1} = 1073nm$ and $\lambda_{res2} = 1377nm$ for dip 1 and dip 2, respectively. From these two resonant wavelength values, the change in resonant wavelength can be calculated as $\Delta\lambda_{res1}$ and $\Delta\lambda_{res2}$ for change in $\Delta n = 0.05$. Shortly, upon the change of RI in the environment by some value Δn, the resonance undergoes a wavelength shift $\Delta\lambda$. This is the principle of plasmonic sensing. A similar phenomenon is observed for the presented device to act like an RI sensor. The diagrammatic demonstration is as shown in Fig. 3.

Apart from the RI values, the λ_{res} depends upon the structural parameters. At some particular values of these parameters, the performance of the sensor could attain its optimum state. The parameter optimization is done as described in the next section.

Device Optimization

The transmittance profile of the presented MIM waveguiding structure is illustrated in Fig. 4a, b when the essential architectural requirements h, w, l_1, l_2, w_1, and w_2 are fitted to be 160 nm, 50 nm, 330 nm, 165 nm, 30 nm, and 30 nm, respectively, for RI ranges between 1.8 and 1.95 and between 2.1 and 2.3 with a step size (Δn) of 0.05. These figures clearly show two distinct modes designated

Fig. 3 Transmittance curve showing the resonance shift

a)

b)

c)

d)
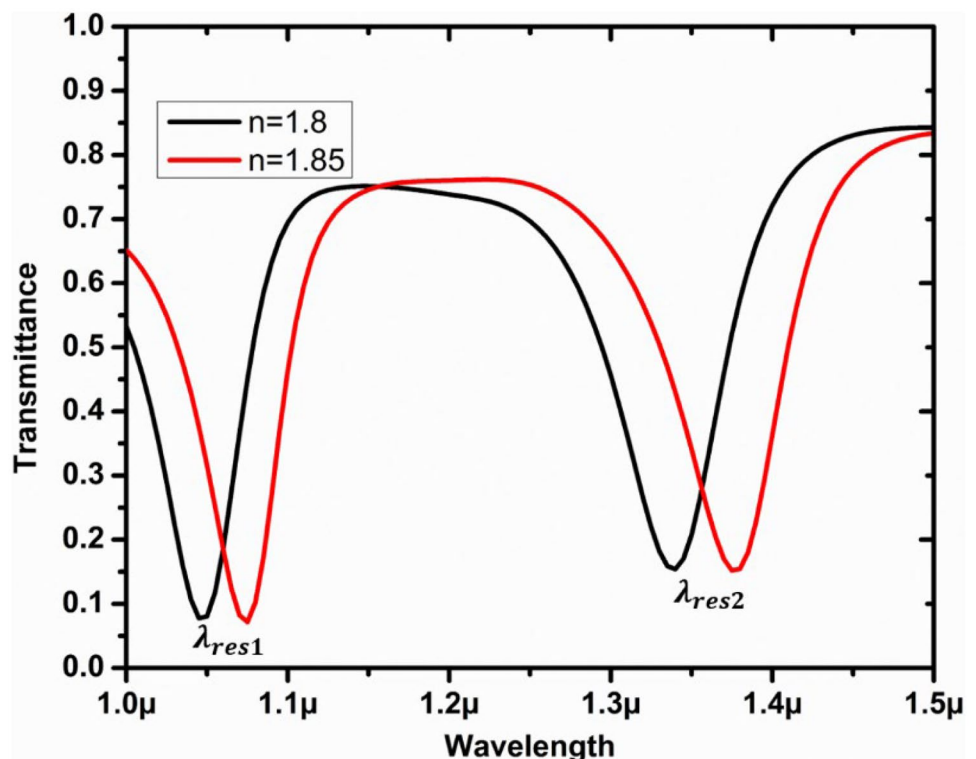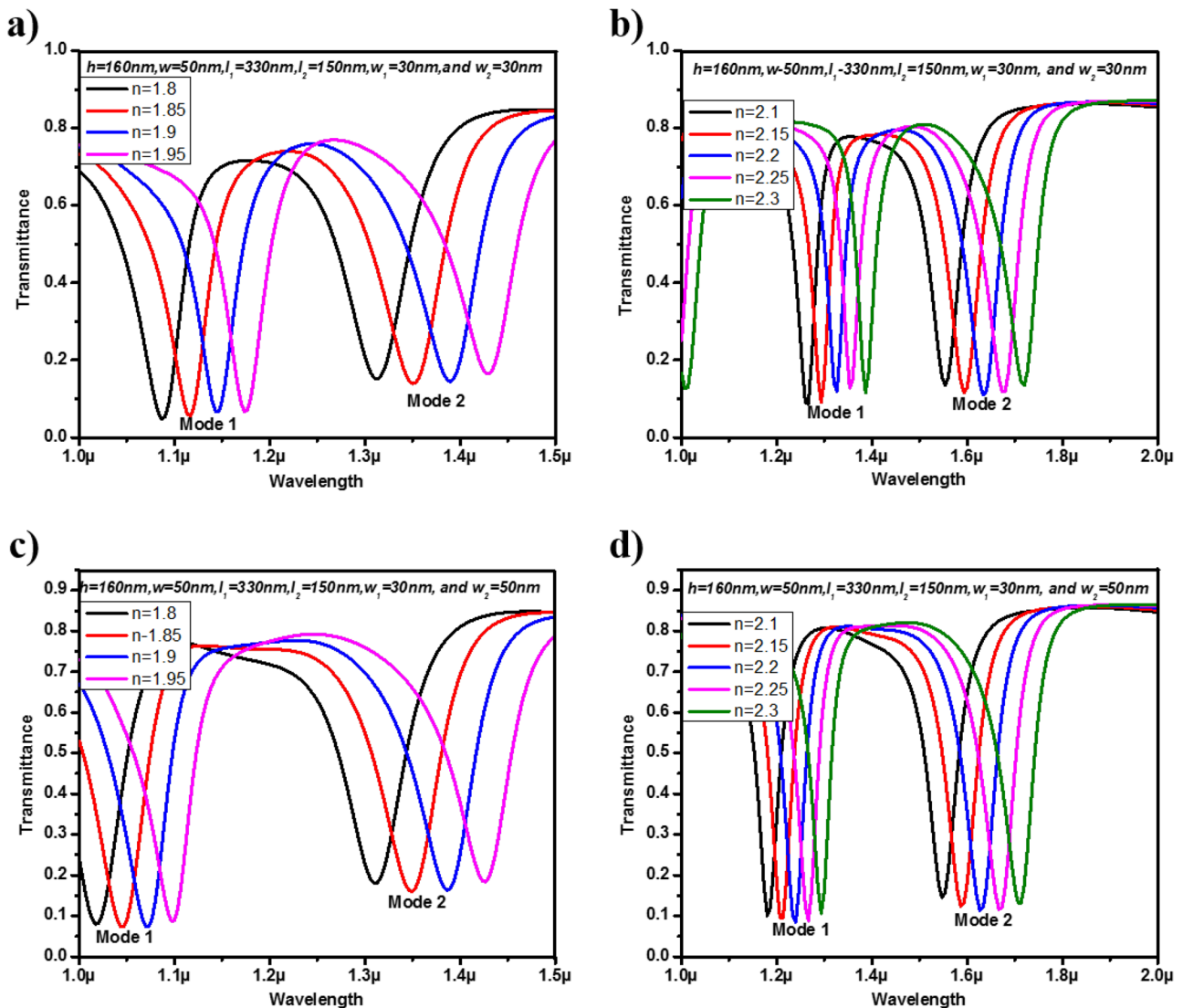
Fig. 4 Transmittance spectra for varying RIs when w_2=30 nm (**a**, **b**) and w_2=50 nm (**c**, **d**)

as mode 1 and mode 2 having two distinct resonance dips occurs at λ_{res}=1085.77 nm and 1312.99 nm at RI = 1.8, respectively. Furthermore, two resonant dips occur for RI = 2.1 at λ_{res}= 1261.44 nm and 1555.55 nm, respectively. The distinct modes are generated due to the silver nanowall formation at the top of WG between the two legs and below the mid-arm of the H-shape cavity [50]. As the fed EM wave travels across the core of WG, the energy of the wave couples with the proposed cavity, the transmittance dips are generated as a result of coupling SPP with two modes such as surface plasma resonance mode and cavity plasmon resonance mode, and finally, some transmittance peaks reach to a low energy level when the resonant condition is satisfied [49]. The depth of these peaks is determined by the various resonant circumstances that originated in the H-shape resonator. By changing the cavity parameters, different resonant conditions have been

generated. First, keeping all other parameters constant, the w_2 is varied from 30 to 60 nm with steps of 10 nm. In this condition, the resonant dips have shown redshift as the RI is incremented from 1.8 to 1.95 and from 2.1 to 2.3 with a Δn of 0.05 as depicted in Fig. 4a–d. Similarly, the resonant dips have shown the red-shift as l_1 is raised from 330 to 360 nm with an increment size of 10 nm.

Depending upon the spectral features of the layout, we can use the proposed design for RI detecting applications. Cavity resonators are generally quick to detect the ambient RI, and as RI increases, their resonant peaks move towards the longer wavelength. The sensitivity is one of the most essential factors used to evaluate the sensing execution. The sensitivity (S) of the RI sensor is defined as the proportion of the alteration in the λ_{res} to the variation in the RI, as given by the succeeding expression [22].

Fig. 5 Spectrum of the transmittance of the structure to illustrate the FWHM
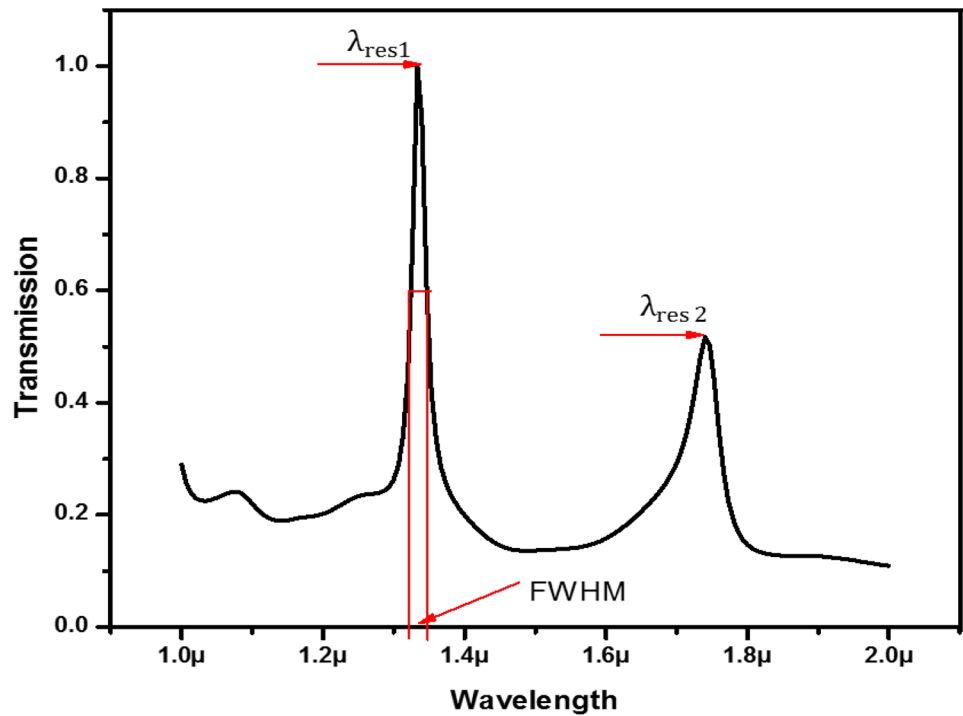
$$S = \frac{\Delta\lambda_{res}}{\Delta n} \qquad (7)$$

The figure of merit (FoM) and quality factor (Q-factor) are two more essential parameters to consider when evaluating a sensor's performance. The FoM is calculated using the formula below [51].

$$FoM = \frac{S}{FWHM\ Bandwidth} \qquad (8)$$

where full-width at half maximum (FWHM) has a bandwidth, which indicates the size of the device. The higher the size of the device, the higher will be the FWHM and results in the lowering of FoM [51]. The Q-factor is mathematically related to λ_{res} and FWHM and is expressed as:

$$Q = \frac{FWHM}{\lambda_{res}} \qquad (9)$$

The FWHM is calculated from the transmission curve as shown in Fig. 5.

The optical characteristics of the proposed design were analyzed based on spectral responses. The spectral characteristic was monitored after stuffing the cavity with several RIs. The intensities are observed from the output port, then they are normalized within the wavelength range of 1000–2000 nm at $n = 1.8$–1.95 and $n = 2.1$–2.3 with $\Delta n = 0.05$. Here, we have observed the influence of w_2 on the resonance wavelength shift that is needed to enhance the performance of the sensor in terms of sensitivity. The resonant wavelengths at the corresponding RIs are noted and summarized in Tables 2, 3, 4, 5, 6, 7, and 8. The respective sensitivities are calculated based on Eq. (7) and summarized on these tables. Tables 2 and 3 summarize the sensitivities of the design for mode 1 having two bands of RIs (the first band is RI = 1.8–1.95 and the second band is RI = 2.1–2.3) with $\Delta n = 0.05$ in

Table 2 RI sensitivities of the presented design for material media ($n = 1.8$ through $n = 1.95$ with the step size of $\Delta n = 0.05$) versus different w_2 (mode 1)

Mode 1								
w_2 (nm)	λres (nm)		S (nm/RIU)	λ_{res} (nm)		S (nm/RIU)	λ_{res} (nm)		S (nm/RIU)
	$n = 1.8$	$n = 1.85$		$n = 1.85$	$n = 1.9$		$n = 1.9$	$n = 1.95$	
30	1085.77	1113.61	556.77	1113.61	1142.85	584.76	1142.85	1173.48	612.75
40	1042.53	1071.77	584.76	1071.77	1101.01	584.76	1101.01	1131.65	612.75
50	1012.97	1039.56	531.76	1039.56	1065.99	528.65	1065.99	1096.62	612.62
60							1030.87	1056.37	509.89

Table 3 RI sensitivities of the presented design for material media (n = 2.1 through n = 2.3 with the step size of $\Delta n = 0.05$) versus different w_2 (mode 1)

Mode 1											
w_2 (nm)	λ_{res}(nm) $n=2.1$	$n=2.15$	S (nm/RIU)	λ_{res}(nm) $n=2.15$	$n=2.2$	S (nm/RIU)	λ_{res}(nm) $n=2.2$	$n=2.25$	S (nm/RIU)	λ_{res}(nm) $n=2.25$	$n=2.3$	S (nm/RIU)
30	1261.44	1294.76	666.37	1294.76	1323.55	575.74	1323.55	1354.73	623.72	1354.73	1388.05	666.37
40	1215.86	1244.65	575.77	1244.65	1278.23	671.67	1278.23	1306.75	570.41	1306.75	1335.54	575.74
50	1177.74	1206.53	575.74	1206.53	1232.65	522.43	1232.65	1263.84	623.72	1263.84	1294.76	618.39
60	1139.36	1165.75	527.77	1165.75	1192.14	527.77	1192.14	1218.26	522.43	1218.26	1247.05	575.74

either band in the case of w_2 which ranges between 30 and 60 nm at the interval size of 10 nm. The $\lambda_{res} = 1142.85$ nm obtained at $n = 1.9$ which shifted to 1173.49 nm for $\Delta n = 0.05$ when $w_2 = 30$nm. The noted sensitivity, in this case, was 612.75 nm/RIU, which is the maximum sensitivity observed in mode 1(RI = 1.8–195). Similarly, Table 2 shows mode 1 with $w_2 = 40$nm. The $\lambda_{res} = 1244.65$nm was achieved at $n = 2.15$ which shifted to 1278.23 nm for $\Delta n = 0.05$. With this shifting, the maximum sensitivity of 672.67 nm/RIU was observed.

Tables 4 and 5 summarize the resonant dips and the respective sensitivity obtained for mode 2 for the RI bands: RI = 1.8–1.95 and RI = 2.1–2.3 with a variation of w_2 from 30 to 60 nm. For the first band of RI, the maximum sensitivity obtained was 839.63 nm/RIU for $w_2 = 50$nm where the $\lambda_{res} = 1388.0$ at $n = 1.9$ shifts to 1428.59 with $\Delta n = 0.05$ (Table 3). Similarly, for the second band of RI, the maximum sensitivity obtained was 863.26 nm/RIU for $w_2 = 30 - 50$nm each for shifting of $n = 2.25 - 2.3$.

Now, the vertical length (l_1) is varied from 330 to 360 nm by keeping $w_2 = 50$nm, where the maximum sensitivity has been observed as discussed before. All other parameters are kept constant. Table 5 summarizes the resonant wavelengths for two modes with $n = 1.8$ and $n = 1.85$. At mode 1, the maximum sensitivity observed was 623.87 nm/RIU when the resonant shift occurred from $\lambda_{res} = 1103.96$nm at $n = 1.8$ to 1135.15 nm with $\Delta n = 0.05$. Similarly, at mode 2, the maximum sensitivity observed was 954.45 nm/RIU when the resonant shift occurred from $\lambda_{res} = 1395.62$nm at $n = 1.8$ to 1443.34 nm with $\Delta n = 0.05$. For both modes to achieve the maximum sensitivity, the l_1 is 360 nm.

The resonant wavelengths and accompanying sensitivities for the following band of RI, i.e., 2.1 to 2.3, are summarized in Tables 7 and 8, where Table 7 is used for mode 1 and Table 8 is used for mode 2. Now, l_1 is adjusted while $w_2 = 50$ nm is maintained, and the cavity is filled with sensing materials with RI ranging from 2.1 to 2.3 in 0.05 step sizes. When the resonant wavelength shifting is from 1309.5 nm at $n = 2.15$ to 1343.10 nm at $n = 2.2$, the greatest sensitivity reached is 671.85 nm/RIU. The supreme sensitivity of 1007.78 nm/RIU was achieved for $l_1 = 350$ nm and $w_2 = 50$nm

in mode 2, where the $\lambda_{res} = 1742.21$ was obtained at $n = 2.25$ and swifts at 1792.60 nm for $\Delta n = 0.05$.

Furthermore, l_2 is varied from 150 to 165 nm with the step size of 5 nm keeping $l_1 = 350$ nm and $w_2 = 50$nm. Although resonant shifts were recorded, the sensitivity could not exceed 960 nm/RIU. The summary of the three important parameters, sensitivity, FoM, and Q-factor for the optimized design ($l_1 = 350$ nm, $w_2 = 50$nm, and $l_2 = 150$ nm) is depicted in Table 9.

The resonant dips are mainly dependent on four factors, as shown in the spectral graphs and the summary of the above-depicted tables: vertical length of the H-shape cavity, l_1; the horizontal length of the H-shape cavity, l_2; the width of the middle arm of the cavity, w_2; and RIs of the sensing substances. The locations of transmittance peaks show a straight relationship with all these aforementioned factors as can be seen from Fig. 6a-d. Since there is a correlation between resonant dip and effective refractive index as given by Eq. (6), i.e., there is a directly proportional association between them, the assessed transmittance scales of the two distinct modes show a redshift with the increment of RI (Fig. 6c, d). Moreover, there is a directly proportional association between the effective length of the resonator and the wavelength corresponding to resonance as defined by Eq. (6). The same linear but direct proportional relationship between the resonance wavelength and l_1 is observed with this design as shown in Fig. 6a. This demonstrates the fact that the effective length of the cavity gets increased due to the increment of the vertical length of the cavity. As illustrated in Fig. 6b, there appears to be an indirect proportional link between the resonant wavelength and w_2. This would be because of the shortening in the effective length of the resonator.

Figure 7a, b depicts the relationship between FWHM and vertical length and the width of the cavity's mid-arm. The graphs depict incremental relationships with both parameters; however, the relationships lack linearity. As the cavity's size grows, so does the number of ions and electrons, resulting in higher collision rates. The plasmon damping is automatically increased as collision rates increase. The FWHM increases as the plasmon damping increases. The non-linear

Table 4 RI sensitivities of the presented design for material media ($n = 1.8$ through $n = 1.95$ with the step size of $\Delta n = 0.05$) versus different w_2 (mode 2)

Mode 2

w_2(nm)	λres (nm)		S (nm/RIU)	λres (nm)		S (nm/RIU)	λ_{res} (nm)		S (nm/RIU)
	$n = 1.8$	$n = 1.85$		$n = 1.85$	$n = 1.9$		$n = 1.9$	$n = 1.95$	
30	1312.99	1350.62	752.72	1350.62	1388.26	752.72	1388.26	1428.85	811.82
40	1310.19	1346.42	724.73	1346.42	1384.21	755.83	1384.21	1424.65	808.71
50	1311.35	1348.98	724.57	1348.98	1388.0	724.57	1388.0	1428.59	839.63
60	1308.66	1345.87	744.06	1345.87	1383.07	744.06	1383.07	1422.16	781.83

relationship suggests that the proposed cavity structure has a reduced number of hardness and density of point defects. The FWHM value provides significant information about the material's surface state. This demonstrates that the FWHM is extremely sensitive to nanostructure variation.

Discussion

Plasmonic devices have a simpler construction and smaller size, which is an interesting feature for their integration along with other nano-size devices at the chip level. Since the proposed device in this paper has compactness in size and simplicity in architecture, it can be easily fabricated. We believe that manufacturing can be done with greater flexibility. The steps for the fabrication process are Au layer deposition, spin coating, E – beam writing, developing, chemical etching, and resist removal [52]. Furthermore, the device's construction is contingent on the device's robustness being estimated. The robustness of a device refers to its tolerance for manufacturing flaws. The geometrical parameters, the parallelism of the cavity walls (the cavity walls are parallel), and the roughness of the cavity wall are all fabrication faults. These defects can be quantified as FWHM. The natures of FWHM plots as against the cavity length and width show the device is tolerant to fabrication defects. FWHM is seen thinner, which indicates the better signal-to-noise ratio we can achieve from the device. The smaller the SNR, the higher the sensitivity of the device. Therefore, this device can be used for sensing different liquids and chemicals whose RIs stand between 1.8–1.95 and 2.1–2.3. Among the two bands of RIs, the change in the liquid crystal lies in the first band, i.e., $n = 1.8$ to 1.95. As a result, this instrument detects changes in liquid crystals. Some birefringent nematic liquid crystals like phenyldi-iodoarsine ($n = 1.85$) [53, 54] can be sensed. Moreover, the fillers used in painting purposes whose RI ranges from 1.8 to 1.9 can also be sensed. For instance, aluminum oxide, antimony pentoxide, calcium carbonate aragonite, magnesium oxide with $n \sim 1.7$ to 1.74 and gadolinium oxide ($n = 1.8$), zinc stannate ($n = 1.9$), and aluminum nitride ($n = 1.9$) [55] are the important fillers that are often used in making the color mixture for painting. At the optimal condition, it has a maximum sensitivity of 1007.78 nm/RIU. This figure is acceptable as compared to previously reported SPPs' waveguide sensors as shown in Table 10.

Apart from sensitivity, the proposed sensor is compared to the reported works in Table 11 based on FoM and Q-factor since these characteristics ensure unique sensing performances.

From Table 11, the results achieved are acceptable as compared to other works. Q-factor is seen higher for Si-based hybrid designs and composite structures [65]. The Q-factor is directly related to the loss of the device. The

Table 5 RI sensitivities of the presented design for material media ($n=2.1$ through $n=2.3$ with the step size of $\Delta n=0.05$) versus different w_2 (mode 2)

Mode 2												
w_2 (nm)	λ_{res}(nm)		S (nm/RIU)	λ_{res}(nm)		S (nm/RIU)	λ_{res}(nm)		S (nm/RIU)	λ_{res}(nm)		S (nm/RIU)
	$n=2.1$	$n=2.15$		$n=2.15$	$n=2.2$		$n=2.2$	$n=2.25$		$n=2.25$	$n=2.3$	
30	1555.44	1593.56	762.33	1593.56	1634.34	815.64	1634.34	1674.86	810.31	1674.86	1718.04	863.62
40	1548.25	1586.36	762.33	1586.36	1627.14	815.64	1627.14	1665.26	762.33	1665.26	1708.44	863.62
50	1555.06	1588.76	673.92	1588.76	1629.54	815.64	1629.54	1667.66	762.33	1667.66	1710.84	863.62
60	1543.45	1586.36	858.29	1586.36	1624.74	767.66	1624.74	1665.26	810.31	1665.26	1706.04	815.64

Table 6 Two peaks of the presented design for material media ($n=1.8$ and $n=1.85$) and their RI sensitivities vs distinct l_1

	Mode 1			Mode 2		
l_1 (nm)	λ_{res}(nm)		S (nm/RIU)	λ_{res}(nm)		S (nm/RIU)
	$n=1.8$	$n=1.85$		$n=1.8$	$n=1.85$	
330	1012.97	1039.56	531.76	1314.15	1350.38	724.57
340	1039.43	1070.36	618.52	1335.90	1374.02	752.5
350	1072.76	1101.56	575.9	1369.22	1407.62	767.83
360	1103.96	1135.15	623.87	1395.62	1443.34	954.45

Table 7 Mode 1 and its RI sensitivities of the presented design for material media ($n=2.1$ through $n=2.3$) versus different l_1

Mode 1												
l_1 (nm)	λ_{res}(nm)		S (nm/RIU)	λ_{res}(nm)		S (nm/RIU)	λ_{res}(nm)		S (nm/RIU)	λ_{res} (nm)		S (nm/RIU)
	$n=2.1$	$n=2.15$		$n=2.15$	$n=2.2$		$n=2.2$	$n=2.25$		$n=2.25$	$n=2.3$	
330	1177.74	1206	575.74	1206	1232.65	522.43	1232.65	1263.84	623.72	1263.84	1294.76	618.39
340	1211.40	1237.80	527.88	1237.80	1268.99	623.86	1268.99	1299.91	618.53	1299.91	1428.70	575.87
350	1247.39	1276.18	575.88	1276.18	1307.11	618.53	1307.11	1335.90	575.88	1335.90	1369.23	666.52
360	1278.59	1309.5	618.53	1309.5	1343.10	671.85	1343.10	1374.02	618.53	1374.02	1405.22	623.87

Table 8 Mode 2 and its RI sensitivities of presented design for material media ($n=2.1$ through $n=2.3$) versus different l_1

Mode 2												
l_1 (nm)	λ_{res}(nm)		S (nm/RIU)	λ_{res}(nm)		S (nm/RIU)	λ_{res}(nm)		S (nm/RIU)	λ_{res} (nm)		S (nm/RIU)
	$n=2.1$	$n=2.15$		$n=2.15$	$n=2.2$		$n=2.2$	$n=2.25$		$n=2.25$	$n=2.3$	
330	1555.06	1588.76	673.92	1588.76	1629.54	815.64	1629.54	1667.66	762.33	1667.66	1710.84	863.6
340	1579.59	1617.98	767.82	1617.98	1658.50	810.49	1658.50	1701.69	863.80	1701.69	1747.01	906.47
350	1615.58	1658.50	858.48	1658.50	1699.29	815.82	1699.29	1742.21	858.48	1742.21	1792.60	1007.78
360	1651.30	1694.50	863.80	1694.50	1739.81	906.47	1739.81	1785.40	911.80	1785.40	1830.73	906.47

higher the Q-factor, the lower will be the loss in the device and vice versa. Therefore, the value of the Q-factor with this design ensures comparatively lower device losses. Although the previously described designs have greater FoM values, their structures are more complex due to their composite character. Since FoM takes into account the impact of peak width on sensing performance, this design offers comparatively wider peaks. One of the major advantages of the proposed sensor is that there is a proper compromise between sensitivity values and other parameters.

From the simulation results, it is seen that the necessary conditions required for sensing applications have been

Table 9 Summary of three parameters of the proposed RI sensor

RI	Mode 1				Mode 2			
	S (nm/RIU)	FWHM (nm)	FoM	Q-factor	S (nm/RIU)	FWHM (nm)	FoM	Q-factor
2.1								
2.15	575.88	24	24	52	858.48	43	20	38
2.2	618.53	21	29	60	815.52	50	16.3	34
2.25	575.88	24	24	54	858.48	60	14.3	28.3
2.3	666.52	24	27	55	1007.78	43	23	40.5

achieved. One of the prominent and foremost conditions that the proposed device exhibit is — it has a powerful redshift in the resonant dips for the small change of RI. The same feature is a foundation for nano-scale sensing applications [22, 23, 46]. Furthermore, because SPPs have their maximal electric field energy contained within the cavity resonator, they are more sensitive to changes in material media or optical RIs [52].
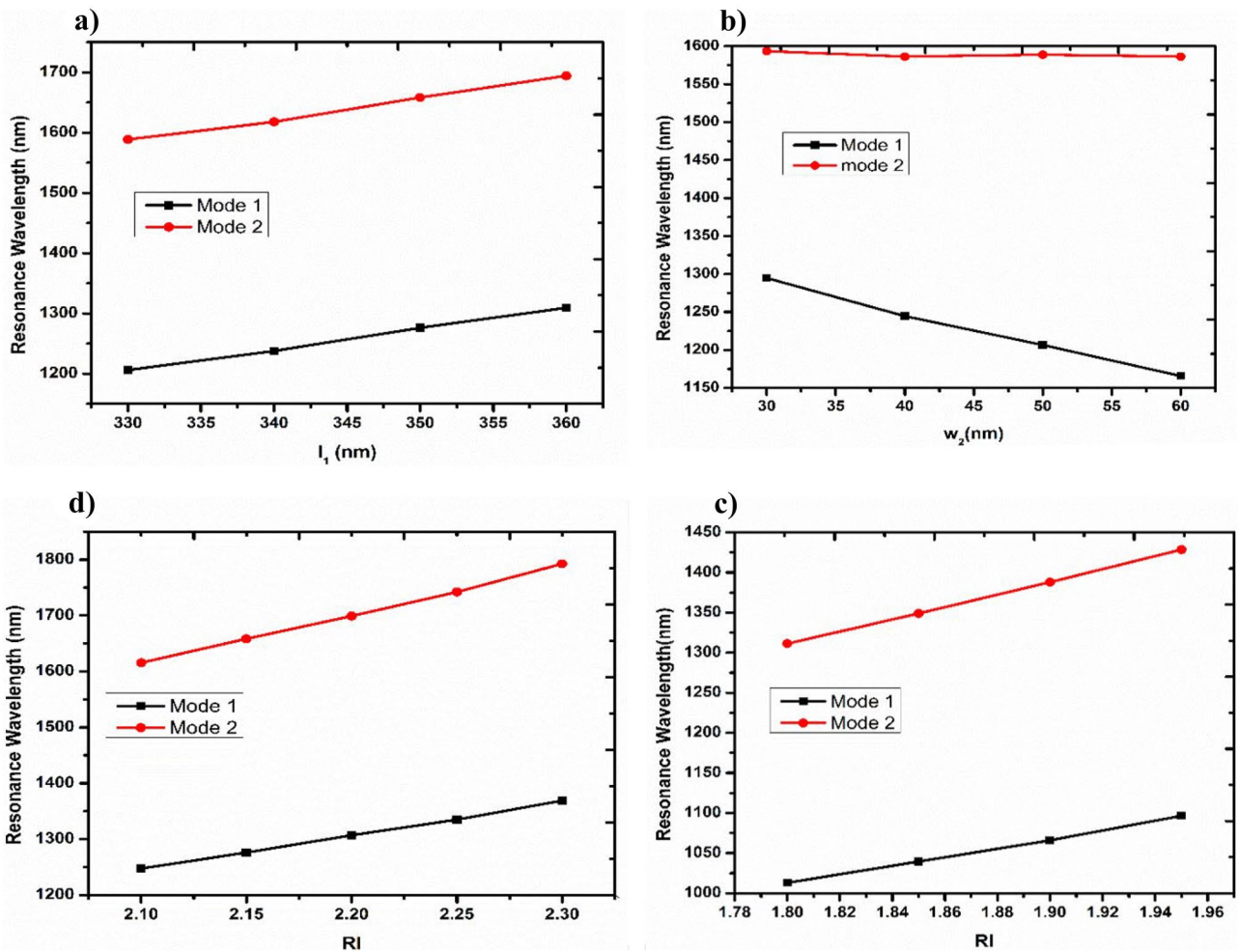
Fig. 6 Plots **a** resonant wavelength versus l_1, **b** resonant wavelength versus w_2, **c** resonant wavelength versus RI for $n = 1.8$ to $n = 1.95$, and **d** resonant wavelength versus RI for $n = 2.1$ to $n = 2.3$ (for two modes)
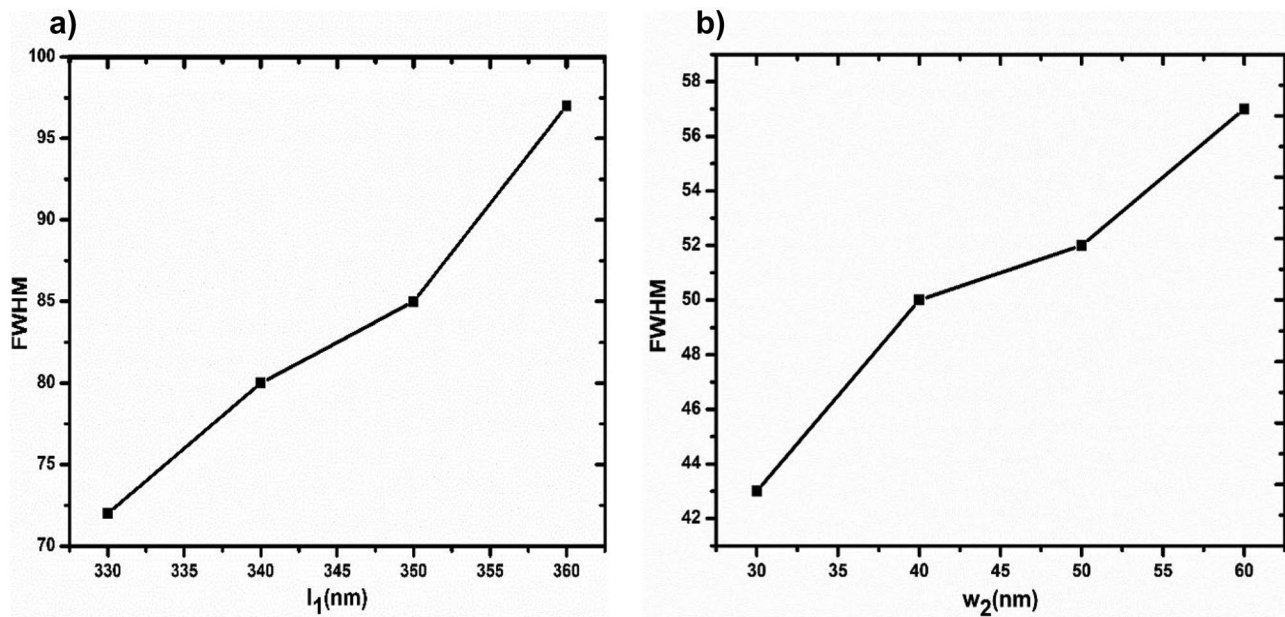
Fig. 7 Plots **a** Full-wave at half maximum versus l_1 **b** Full-wave at half maximum versus w_2

Table 10 Differentiation of several recently reported plasmonics sensors from our work in terms of sensitivity

Reference	Sensitivity (nm/RIU)
[56]	494
[57]	595
[58]	671
[59]	718
[60]	800
[61]	1000
Our work	1007.78
[27]	1125
[62]	1303

Table 11 Comparison of our results with the previously reported works based on FoM and Q-factor

References	FoM	Q-factor
[42]	25	31.5
[44]	211.3	–
[51]	287.9	–
[63]	36	42.28
[64]	203.8	–
[65]	133	`132.8
[66]	19.5	–
Our work	29	60

Concluding Remarks

A nano-sized, metal-dielectric-metal structure-based sensitive refractive index sensor with 180nm × 400nm size is modeled and scrutinized by the finite element method. The device design consists of an H-shaped cavity linked with the main waveguide. Device parameters like the width, length of mid-arm, vertical length of the cavity, etc., and material media inside the cavity are varied for optimizing the device performance. At optimized conditions, maximal sensitivity of 1007.78 nm/RIU is found which is remarkable for plasmonic sensors having a single structure that is coupled to the main waveguide. The proposed device's figure of merit and quality factor are also investigated. The proposed design is thought to be simple, compact, and robust towards the fabrication defects, allowing it to be used for sensing applications (or to measure refractive index changes), and it can undoubtedly be incorporated at the chip level as an on-chip optical nanosensor.

Declarations

Ethics Approval Not applicable.

Consent to Participate Not applicable.

Consent for Publication Not applicable.

Conflict of Interest The authors declare no competing interests.

References

1. Dragoman M, Dragoman D (2008) Plasmonics : applications to nanoscale terahertz and optical devices 32:1–41. https://doi.org/10.1016/j.pquantelec.2007.11.001

2. Zhang J, Zhang L, Xu W (2012) Surface plasmon polaritons: physics and applications. J Phys D Appl Phys. https://doi.org/10.1088/0022-3727/45/11/113001

3. Maier SA (2007) Chapter 2 surface plasmon polaritons at metal. Plasmon Fundam Appl 0:1–2

4. Lin X-S, Huang X-G (2008) Tooth-shaped plasmonic waveguide filters with nanometeric sizes. Opt Lett 33:2874. https://doi.org/10.1364/ol.33.002874

5. Zhang Q, Huang X-G, Lin X-S, Tao J, Jin X-P (2009) A sub-wavelength coupler-type MIM optical filter. Opt Express 17:7549. https://doi.org/10.1364/oe.17.007549

6. Jin XP, Huang XG, Tao J, Lin XS, Zhang Q (2010) A novel nanometeric plasmonic refractive index sensor. IEEE Trans Nanotechnol 9:134–137. https://doi.org/10.1109/TNANO.2009.2038909

7. Tao J, Wang QJ, Huang XG (2011) All-optical plasmonic switches based on coupled nano-disk cavity structures containing nonlinear material. Plasmonics 6:753–759. https://doi.org/10.1007/s11468-011-9260-1

8. Yang R, Lu Z (2012) Subwavelength plasmonic waveguides and plasmonic materials. Int J Opt. https://doi.org/10.1155/2012/258013

9. Onbasli MC, Okyay AK (2010) Nanoantenna couplers for metal-insulator-metal waveguide interconnects. Plasmon Met Nanostructures Their Opt Prop VIII 7757:77573R. https://doi.org/10.1117/12.876177

10. Rahman ZU, Krishna KM, Reddy KK, Babu MV, Mirza S, Fathima SY (2018) Ultra wide band band-pass filters using plasmonic MIM waveguide based ring resonators, IEEE Photonics Technol Lett PP (2018) 1. https://doi.org/10.1109/LPT.2018.2866966

11. Ebadi SM, Member S, Ebadi SM, Member S, Örtegren J (2020) A multipurpose and highly-compact plasmonic filter based on metal-insulator-metal a multipurpose and highly-compact plasmonic filter based on 12. https://doi.org/10.1109/JPHOT.2020.2974959

12. Chauhan D, Kumar A, Adhikari R, Saini RK, Chang SH, Dwivedi RP (2021) High performance vanadium dioxide based active nano plasmonic filter and switch. Optik (Stuttg) 225:165672. https://doi.org/10.1016/j.ijleo.2020.165672

13. Taheri AN, Kaatuzian H (2015) Numerical investigation of a nano-scale electro-plasmonic switch based on metal-insulator-metal stub filter. Opt Quantum Electron 47:159–168. https://doi.org/10.1007/s11082-014-9895-1

14. Wen K, Yan L, Pan W, Luo B, Guo Z, Guo Y (2012) Wavelength demultiplexing structure based on a plasmonic metal-insulator-metal waveguide. J Opt (United Kingdom) 14. https://doi.org/10.1088/2040-8978/14/7/075001

15. Chauhan D, Mola GT, Dwivedi RP (2020) An ultra-compact plasmonic modulator/switch using VO2 and elasto-optic effect. Optik (Stuttg) 201:163531. https://doi.org/10.1016/j.ijleo.2019.163531

16. Dwivedi RP, Lee HS, Song JH, An S, Lee EH (2011) Plasmonic modulator utilizing three parallel metal-dielectric-metal waveguide directional coupler and elasto-optic effects. Opt Commun 284:1418–1423. https://doi.org/10.1016/j.optcom.2010.10.038

17. Wahsheh RA, Lu Z, Abushagur MAG (2009) Nanoplasmonic couplers and splitters. Opt Express 17:19033. https://doi.org/10.1364/oe.17.019033

18. Guo Y, Yan L, Pan W, Luo B, Wen K, Guo Z, Li H, Luo X (2011) A plasmonic splitter based on slot cavity. Opt Express 19:13831. https://doi.org/10.1364/oe.19.013831

19. Wu T, Liu Y, Yu Z, Peng Y, Shu C, Ye H (2014) The sensing characteristics of plasmonic waveguide with a ring resonator. Opt Express 22:7669. https://doi.org/10.1364/oe.22.007669

20. Binfeng Y, Guohua H, Ruohu Z, Yiping C (2014) Design of a compact and high sensitive refractive index sensor base on metal-insulator-metal plasmonic Bragg grating. Opt Express 22:28662. https://doi.org/10.1364/oe.22.028662

21. Rakhshani MR, Mansouri-Birjandi MA (2017) High sensitivity plasmonic refractive index sensing and its application for human blood group identification. Sens Actuators B Chem 249:168–176. https://doi.org/10.1016/j.snb.2017.04.064

22. Butt MA, Khonina SN, Kazanskiy NL (2021) Metal-insulator-metal nano square ring resonator for gas sensing applications. Waves Random Complex Media 31:146–156. https://doi.org/10.1080/17455030.2019.1568609

23. Butt MA, Kazanskiy NL, Khonina SN (2020) Highly sensitive refractive index sensor based on plasmonic bow tie configuration. Photonic Sens 10:223–232. https://doi.org/10.1007/s13320-020-0588-z

24. Chen Z, Yu L (2014) Multiple Fano resonances based on different waveguide modes in a symmetry breaking plasmonic system. IEEE Photonics J. https://doi.org/10.1109/JPHOT.2014.2368779

25. Chen Z, Cao X, Song X (2015) Side-coupled cavity-induced Fano resonance and its application in nanosensor. https://doi.org/10.1007/s11468-015-0035-y

26. Zhang Y, Li S, Zhang X, Chen Y, Wang L, Zhang Y, Yu L (2016) Evolution of Fano resonance based on symmetric/asymmetric plasmonic waveguide system and its application in nanosensor. Opt Commun 370:203–208. https://doi.org/10.1016/j.optcom.2016.03.001

27. Tang Y, Zhang Z, Wang R, Hai Z, Xue C, Zhang W, Yan S (2017) Refractive index sensor based on fano resonances in metal-insulator-metal waveguides coupled with resonators. Sensors (Switzerland). https://doi.org/10.3390/s17040784

28. Deng Y, Cao G, Yang H, Li G, Chen X, Lu W (2017) Tunable and high-sensitivity sensing based on Fano resonance with coupled plasmonic cavities. Sci Rep 7:2–9. https://doi.org/10.1038/s41598-017-10626-1

29. Zhang Y, Kuang Y, Zhang Z, Tang Y, Han J, Wang R, Cui J, Hou Y, Liu W (2019) High-sensitivity refractive index sensors based on Fano resonance in the plasmonic system of splitting ring cavity-coupled MIM waveguide with tooth cavity. Appl Phys A. https://doi.org/10.1007/s00339-018-2283-0

30. Wang S, Zhao T, Yu S, Ma W (2020) High-performance nano-sensing and slow-light applications based on tunable multiple Fano resonances and EIT-like effects in coupled plasmonic resonator system. IEEE Access 8:40599–40611. https://doi.org/10.1109/ACCESS.2020.2974491

31. Xiao G, Xu Y, Yang H, Ou Z, Chen J, Li H, Liu X, Zeng L, Li J (2021) High sensitivity plasmonic sensor based on fano resonance with inverted u-shaped resonator. Sensors (Switzerland) 21:1–12. https://doi.org/10.3390/s21041164

32. Chauhan D, Adhikari R, Saini RK, Chang SH, Dwivedi RP (2020) Subwavelength plasmonic liquid sensor using Fano resonance in a ring resonator structure. Optik (Stuttg) 223:165545. https://doi.org/10.1016/j.ijleo.2020.165545

33. Baqir MA, Farmani A, Fatima T, Raza MR, Shaukat SF, Mir A (2018) Nanoscale, tunable, and highly sensitive biosensor utilizing hyperbolic metamaterials in the near-infrared range. Appl Opt 57:9447. https://doi.org/10.1364/ao.57.009447

34. Baqir MA (2019) Wide-band and wide-angle, visible- and near-infrared metamaterial-based absorber made of nanoholed tungsten thin film. Opt Mater Express 9:29–31. https://doi.org/10.1364/OME.9.002358

35. Naveed MA, Bilal RMH, Baqir MA, Bashir MM, Ali MM, Rahim AA (2021) Ultrawideband fractal metamaterial absorber made of

nickel operating in the UV to IR spectrum. Opt Express 29:42911. https://doi.org/10.1364/oe.446423

36. Bilal RMH, Baqir MA, Iftikhar A, Naqvi SA, Mughal MJ, Ali MM (2022) Polarization-controllable and angle-insensitive multi-band Yagi-Uda-shaped metamaterial absorber in the microwave regime. Opt Mater Express 12:798. https://doi.org/10.1364/ome.451073

37. Adhikari R, Chauhan D, Mola GT, Dwivedi RP (2021) A review of the current state-of-the-art in Fano resonance-based plasmonic metal-insulator-metal waveguides for sensing applications. Opto-Electronics Rev 29:148–166. https://doi.org/10.24425/opelre.2021.139601

38. Adhikari R, Sbeah Z, Chauhan D, Chang SH, Dwivedi RP (2022) A voyage from plasmonic to hybrid waveguide refractive index sensors based on wavelength interrogation Technique: a Review. Brazilian J Phys 52:61. https://doi.org/10.1007/s13538-022-01064-0

39. Xie YY, Huang YX, Zhao WL, Xu WH, He C (2015) A novel plasmonic sensor based on metal-insulator-metal waveguide with side-coupled hexagonal cavity. IEEE Photonics J 7(2):1–12. https://doi.org/10.1109/JPHOT.2015.2419635

40. Chen L, Liu Y, Yu Z, Wu D, Ma R, Zhang Y, Ye H (2016) Numerical analysis of a near-infrared plasmonic refractive index sensor with high figure of merit based on a fillet cavity. Opt Express 24:9975. https://doi.org/10.1364/oe.24.009975

41. Rakhshani MR, Mansouri-Birjandi MA (2016) High-sensitivity plasmonic sensor based on metal-insulator-metal waveguide and hexagonal-ring cavity. IEEE Sens J 16:3041–3046. https://doi.org/10.1109/JSEN.2016.2522560

42. Butt MA, Khonina SN, Kazanskiy NL (2019) Plasmonic refractive index sensor based on metal–insulator-metal waveguides with high sensitivity. J Mod Opt 66:1038–1043. https://doi.org/10.1080/09500340.2019.1601272

43. Butt MA, Khonina SN, Kazanskiy NL (2019) Plasmonic refractive index sensor based on M-I-M square ring resonator. Int Conf Comput Electron Electr Eng ICE Cube 2018:1–4. https://doi.org/10.1109/ICECUBE.2018.8610998

44. Danaie M, Shahzadi A (2019) Design of a high-resolution metal–insulator–metal plasmonic refractive index sensor based on a ring-shaped si resonator. Plasmonics 14:1453–1465. https://doi.org/10.1007/s11468-019-00926-9

45. Li X, Zhang Z, Guo F, Huang Y, Zhang B, Zhang L, Yang Q, Tan Y, Liu X, Bai H, Song Y (2019) Tunable plasmonically induced reflection in HRR-coupled MIM waveguide structure. Optik (Stuttg) 199:163353. https://doi.org/10.1016/j.ijleo.2019.163353

46. Al Mahmud R, Faruque MO, Sagor RH (2021) A highly sensitive plasmonic refractive index sensor based on triangular resonator. Opt Commun 483:126634. https://doi.org/10.1016/j.optcom.2020.126634

47. Kazanskiy NL, Khonina SN, Butt MA (2020) Plasmonic sensors based on metal-insulator-metal waveguides for refractive index sensing applications: a brief review. Phys E Low-Dimens Syst Nanostructures 113798. https://doi.org/10.1016/j.physe.2019.113798

48. Zafar R, Salim M (2015) Enhanced figure of merit in Fano resonance-based plasmonic refractive index sensor. IEEE Sens J 15:6313–6317. https://doi.org/10.1109/JSEN.2015.2455534

49. Chou Chau YF, Chou Chao CT, Huang HJ, Kumara NT, Lim CM CM, Chiang HP (2019) Ultra-high refractive index sensing structure based on a metal-insulator-metal waveguide-coupled T-shape cavity with metal nanorod defects. Nanomaterials. https://doi.org/10.3390/nano9101433

50. Butt MA, Khonina SN, Kazanskiy NL (2019) A multichannel metallic dual nano-wall square split-ring resonator: design analysis and applications. Laser Phys Lett. https://doi.org/10.1088/1612-202X/ab5574

51. Rahmatiyar M, Danaie M, Afsahi M (2020) Employment of cascaded coupled resonators for resolution enhancement in plasmonic refractive index sensors. Opt Quantum Electron. https://doi.org/10.1007/s11082-020-02266-z

52. Kazanskiy NL, Butt MA, Khonina SN (2020) Nanodots decorated MIM semi-ring resonator cavity for biochemical sensing applications. Photonics Nanostructures - Fundam Appl 42:100836. https://doi.org/10.1016/j.photonics.2020.100836

53. Laskar JM, Kumar PS, Herminghaus S, Daniels KE, Schröter M (2016) High refractive index immersion liquid for superresolution 3D imaging using sapphire-based aplanatic numerical aperture increasing lens optics. 55(12):3165–3169

54. Kang S, Nakajima S, Arakawa Y, Konishi G, Watanabe J (2013) Large extraordinary refractive index in highly birefringent nematic liquid crystals of dinaphthyldiacetylene-based materials. J Materials Chem. 27:4222-4226. https://doi.org/10.1039/c3tc30640b

55. Wypych G (2016) Physical properties of fillers and filled materials. In: Wypych G (ed) Handb Fill, Fourth Ed. ChemTec Publishing p 373–413. https://doi.org/10.1016/B978-1-895198-91-1.50007-5

56. Xiang L, Huang L (2020) High-sensitivity complex refractive index sensor by designing a slot-waveguide side-coupled Fano resonant cavity. Opt Commun 475:126298. https://doi.org/10.1016/j.optcom.2020.126298

57. Zhang Z, Luo L, Xue C, Zhang W, Yan S (2016) Fano resonance based on metal-insulator-metal waveguide-coupled double rectangular cavities for plasmonic nanosensors. Sensors (Switzerland) 16:22–24. https://doi.org/10.3390/s16050642

58. Wang Q, Ouyang Z, Sun Y, Lin M, Liu Q, Zheng G, Fan J (2018). Tunable nanosensor based on Fano resonances created by changing the deviation angle of the metal core in a plasmonic cavity. https://doi.org/10.3390/s18041026

59. Zhao X, Zhang Z, Yan S (2017) Tunable Fano resonance in asymmetric MIM waveguide structure. Sensors (Switzerland). https://doi.org/10.3390/s17071494

60. Liu G, Liu Z, Liu G, Fu X (2020) Plasmonic sensors with an ultra-high figure of merit. Nanotechnology 31:11. https://doi.org/10.1088/1361-6528/ab5a00

61. Shi X, Ma L, Zhang Z, Tang Y, Zhang Y, Han J, Sun Y (2018) Dual Fano resonance control and refractive index sensors based on a plasmonic waveguide-coupled resonator system. Opt Commun 427:326–330. https://doi.org/10.1016/j.optcom.2018.06.042

62. Jina L, Chen J, Liu X, Tian H, Wang J, Cui J, Rohimah S (2021) Optical sensing based on multimode Fano resonances in metal-insulator-metal waveguide systems with X-shaped resonant cavities. 60:5312–5319

63. Zubaidah binti Haji Juma S, Chao CT, Chau YF, Mahadi AH, Kooh MR, Kumara NT, Chiang HP (2021) Plasmonic refractive index sensor based on the combination of rectangular and circular resonators including baffles. Chinese J Phys 71:286–299. https://doi.org/10.1016/j.cjph.2021.02.006

64. Zhang Z, Yang J, He X, Zhang J, Huang J, Chen D, Han Y (2018) Plasmonic refractive index sensor with high figure of merit based on concentric-rings resonator. Sensors (Switzerland). https://doi.org/10.3390/s18010116

65. Amoosoltani N, Mehrabi K, Zarifkar A, Farmani A, Yasrebi N (2021) Double-ring resonator plasmonic refractive index sensor utilizing dual-band unidirectional reflectionless propagation effect. Plasmonics 16:1277–1285. https://doi.org/10.1007/s11468-021-01395-9

66. Rakhshani MR (2020) Tunable and sensitive refractive index sensors by plasmonic absorbers with circular arrays of nanorods and nanotubes for detecting cancerous cells. Plasmonics 15:2071–2080. https://doi.org/10.1007/s11468-020-01237-0